Centrality Dependent Particle Production at $y = 0$ and $y \sim 1$ in Au+Au Collisions at $\sqrt{s_{NN}} = 200$ GeV

I. Arsene,[10] I. G. Bearden,[7] D. Beavis,[1] C. Besliu,[10] B. Budick,[6] H. Bøggild,[7] C. Chasman,[1] C. H. Christensen,[7] P. Christiansen,[7] J. Cibor,[3] R. Debbe,[1] E. Enger,[12] J. J. Gaardhøje,[7] M. Germinario,[7] K. Hagel,[8] H. Ito,[1] A. Jipa,[10] F. Jundt,[2] J. I. Jørdre,[9] C. E. Jørgensen,[7] R. Karabowicz,[4] E. J. Kim,[1,11] T. Kozik,[4] T. M. Larsen,[12] J. H. Lee,[1] Y. K. Lee,[5] S. Lindal,[12] R. Lystad,[9] G. Løvhøiden,[12] Z. Majka,[4] A. Makeev,[8] M. Mikelsen,[12] M. Murray,[8,11] J. Natowitz,[8] B. Neumann,[11] B. S. Nielsen,[7] D. Ouerdane,[7] R. Płaneta,[4] F. Rami,[2] C. Ristea,[10] O. Ristea,[10] D. Röhrich,[9] B. H. Samset,[12] D. Sandberg,[7] S. J. Sanders,[11] R. A. Scheetz,[1] P. Staszel,[7] T. S. Tveter,[12] F. Videbæk,[1] R. Wada,[8] Z. Yin,[9] and I. S. Zgura[10]

(BRAHMS Collaboration)

[1] *Brookhaven National Laboratory, Upton, New York 11973*
[2] *Institut de Recherches Subatomiques and Université Louis Pasteur,Strasbourg, France*
[3] *Institute of Nuclear Physics, Krakow, Poland*
[4] *Smoluchkowski Inst. of Physics, Jagiellonian University, Krakow, Poland*
[5] *Johns Hopkins University, Baltimore, Maryland 21218, USA*
[6] *New York University, New York, New York 10003, USA*
[7] *Niels Bohr Institute, Blegdamsvej 17, University of Copenhagen, Copenhagen 2100, Denmark*
[8] *Texas A&M University, College Station, Texas, 17843, USA*
[9] *University of Bergen, Department of Physics, Bergen, Norway*
[10] *University of Bucharest, Romania*
[11] *University of Kansas, Lawrence, Kansas 66045, USA*
[12] *University of Oslo, Department of Physics, Oslo, Norway*

(Dated: March 2, 2005)

Particle production of identified charged hadrons, $\pi^{\pm}$, $K^{\pm}$, p, and $\bar{p}$ in Au+Au collisions at $\sqrt{s_{NN}} = 200$ GeV has been studied as a function of transverse momentum and collision centrality at $y = 0$ and $y \sim 1$ by the BRAHMS experiment at RHIC. Significant collective transverse flow at kinetic freeze-out has been observed in the collisions. The magnitude of the flow rises with the collision centrality. Proton and kaon yields relative to the pion production increase strongly as the transverse momentum increases and also increase with centrality. Particle yields per participant show a weak dependence on the centrality for all particle species. Hadron production remains relatively constant within one unit around midrapidity in Au+Au collisions at $\sqrt{s_{NN}} = 200$ GeV.

PACS numbers: 25.75.Dw

I. INTRODUCTION

The primary goal of the relativistic heavy-ion collider (RHIC) is to create and study matter at extremely high energy density. It is hypothesized that at the energy densities reached in central Au+Au reactions at RHIC, the matter created is composed of de-confined colored objects [1–3]. A summary of the results and opinions of the four experimental collaborations on the status of achieving this goal can be found in their "White Papers" [4–7]. We expect that the signals of any de-confined phase should be strongest for larger systems. Testing this hypothesis requires studying particle production as a function of centrality. The particle distributions in transverse momentum and rapidity may provide a key to understanding any non-hadronic effects that might appear in central nucleus-nucleus collisions.

Pions, kaons, protons and antiprotons are the most abundantly produced particles in the high-energy, heavy-ion collisions, and they carry information about the bulk properties of the nuclear matter created from the collisions.

Pions, being the lightest of the produced hadrons are thus the most copiously produced, and their numbers can be related to the entropy density of the emitting source. Kaons carry a significant fraction of the total strangeness produced [8]. Protons and antiprotons provide an experimental tool for measuring baryon production and allow us to explore baryon transport from beam rapidity toward mid-rapidity [9, 10]. The global thermodynamic properties and collective motion of the system at the kinetic freeze-out point can be deduced albeit in a model dependent way, from transverse momentum spectra as a function of rapidity and centrality [11].

In this paper, we present transverse momentum spectra, yields, and ratios for identified charged hadrons ($\pi^{\pm}$, $K^{\pm}$, p, $\bar{p}$) obtained with the BRAHMS mid-rapidity spectrometer. We have measured these spectra for $y = 0$ and $y \sim 1$ as a function of collision centrality. The data presented here are available at [12, 13].

II. EXPERIMENTAL DETAILS

The BRAHMS experiment consists of two movable magnetic spectrometer arms, the Mid-Rapidity Spectrometer (MRS) and the Forward Spectrometer (FS), and global detectors for event characterization.

In order to characterize the centrality of collisions, a multiplicity array (MA) consisting of a coaxial arrangement of Si strip detectors and scintillator tiles surrounding the intersection region is employed. Si strip detectors and scintillator tiles give independent measurement of charged-particle multiplicities allowing the two measurements to be averaged in the final determination. The pseudo-rapidity coverage of the MA is approximately $-2.2 < \eta < 2.2$ [14, 15]. The centrality selection is obtained by developing minimum-bias trigger events, which are defined using two Zero Degree Calorimeters (ZDC), requiring energy deposit equivalent to one neutron in each of the two detectors and also requiring a signal in the MA to reject Coulomb dissociation events [14, 16]. Figure 1 shows the charged-particle multiplicity distribution for minimum-bias events in $-2.2 < \eta < 2.2$. The lines on the plot indicate four centrality windows in the analysis, 0−10%, 10−20%, 20−40%, and 40−60%, where 0% corresponds to the most central events.

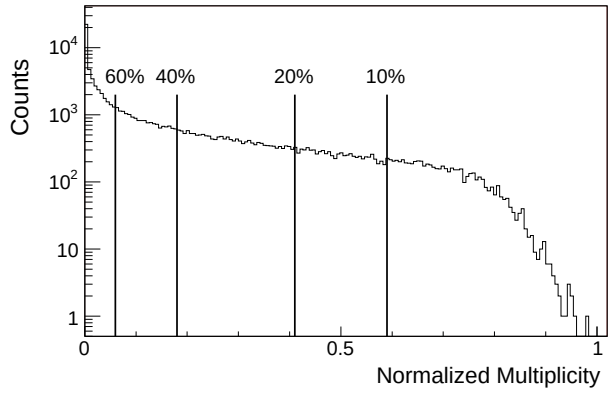

FIG. 1: MA array multiplicity distribution. Lines show the limits for indicated centralities.

The number of participating nucleons (N_{part}) in Table I are estimated using the Glauber Monte-Carlo HIJING calculation [17]. More peripheral collision events were not included in this paper because of limited statistics.

Centrality	$\langle N_{part} \rangle$
$0-10\%$	328 ± 6
$10-20\%$	239 ± 10
$20-40\%$	140 ± 11
$40-60\%$	62 ± 10

TABLE I: The number of participant nucleons N_{part} estimated from the HIJING model [17].

The uncertainty in determining centrality from the multiplicity distribution was estimated to be $\pm 1.7\%$ for the most central bin and $\pm 9.4\%$ for the most peripheral bin. The fraction of the inclusive yield lost by the minimum-bias trigger is estimated to be about 4% and is corrected for. The location of the collision vertex was determined to an accuracy of 0.7 cm using Beam-Beam Counters (BBC) [16]. The BBCs are located 2.2 m on either side of the nominal interaction point and also provide a start time (T0) for time-of-flight measurement.

The MRS is a single-dipole-magnet spectrometer which, by rotating about the nominal collision points, provides the angular coverage of $30^\circ < \theta < 95^\circ$, where θ is the polar angle with respect to the beam axis. The MRS contains two time projection chambers (TPCs), TPM1 and TPM2, which determine the three dimensional trajectories of the charged particles through the spectrometer. Between the two TPCs there is a dipole magnet (D5) for momentum determination. This assembly is followed by a highly segmented scintillator time-of-flight wall (TOFW).

The BRAHMS TPCs are located at a distance 0.95 m (TPM1) and 2.85 m (TPM2) from the interaction point. Each TPC is a rectangular box filled with 90% Ar and 10% CO_2. The ionization produced by charged particles is collected on an anode grid. This grid is divided along the particle path into 12 rows (TPM1) and 20 rows (TPM2). Each row has 96 pads (TPM1) and 144 pads (TPM2) transverse to the direction of a normal-incident particle. The mapping of row, pad, and drift time leads to three-dimensional space points. The averaged resolutions measured from track residuals are 310−387 μm for X (pad) and 427−490 μm for Y (time). Details can be found in Ref. [16, 18–20].

Track reconstruction starts by finding straight-line track segments in the TPCs. The reconstructed straight tracks are joined inside the analyzing magnet by taking an effective edge approximation, and the momentum associated with the track is calculated from the vertical magnet field, the length of the magnet field, the polar angle of the track with respect to the matching plane, and the averaged vertical slope of tracks. Once the momentum is known the reconstructed tracks are projected toward the beam axis and checked for consistency with the collision vertex determined using BBCs. For this analysis we only use tracks that project to within ± 12.5 cm of the nominal vertex in the horizontal plane.

The momentum resolution of the spectrometer can be inferred from the width of our mass-squared distributions since $m^2 = p^2[(ct/l)^2 - 1]$, where c is the velocity of light, l the track path length, and t is the time-of-flight whose resolution is measured independently. The extracted resolutions were fit to the form $(\delta p/p)^2 = (c_{res}p)^2 + (c_{multi}/\beta)^2$, where c_{res} is the contribution from the intrinsic angular resolution of the tracking detectors and c_{multi} is the resolution from multiple scattering. The best fit is given by $c_{res} \sim 0.014$ (corresponding to 2.1 μrad bending angle resolution) and $c_{multi} \sim 0.01$. Fig-

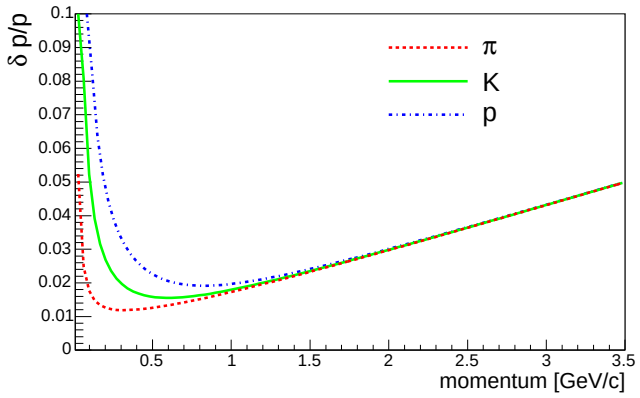

FIG. 2: Momentum resolution $\delta p/p$ calculated for the MRS 90° setting as a function of momentum with a magnetic field of 6 kG. The curves are obtained from parametrization of the mass resolution $\sigma^2_{m^2}$. At low momentum multiple scattering dominates the resolution while above 1GeV the angular resolution of the spectrometers is the most important effect.

ure 2 shows resolution curves based on this fit for pions, kaons and protons when the D5 magnet is set to 6 kG. For the data presented in this paper the momentum resolution lies between 2 and 8%.

Particle Identification (PID) is based on time of flight data from the TOFW, ($\sigma_t \approx 80$ ps) with the start time taken from the BBC ($\sigma_t \approx 35$ ps). Final mass identification PID is based on cuts in the m^2 vs. p space, as shown in Fig. 3. The cut boundaries are set at $\pm 3\sigma$ from the mean m^2 values. The kaon contamination within the pion sample is less than 1%. TOFW provides π/K separation to the momenta of 2 GeV/c and K/p separation to the momenta of 3 GeV/c.

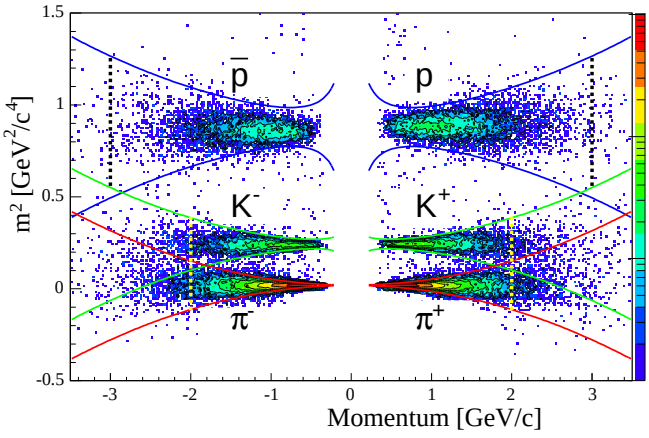

FIG. 3: Mass-squared distribution in TOFW as a function of reconstructed particle momentum obtained from tracking in TPCs through the D5 magnet at $y = 0$. The curves in the figure are PID boundaries set at $\pm 3\sigma_{m^2}$ from the mean m^2 of the particle. The dotted lines indicate the momentum cuts for particle separation.

The data presented here were collected with the MRS at 90°, for $y \sim 0$ ($-0.1 < y < 0.1$) and at $45° - 35°$ for $y \sim 1$ ($-0.7 < y < 1.1$). The same rapidity interval is used for each particle.

From the number identified particles, invariant differential yields are obtained from several spectrometer settings for different collision centralities. The invariant yields are corrected for geometrical acceptance and the efficiencies for detecting particles in the spectrometer.

Geometrical acceptance factors are obtained from the GEANT [21] simulation package BRAG (BRAHMS Analysis Geant), which is based upon the geometry and tracking capabilities of the the BRAHMS experimental setup. The acceptance correction is calculated for each MRS setting and five different vertex windows covering the MRS track vertex ranges in the analysis.

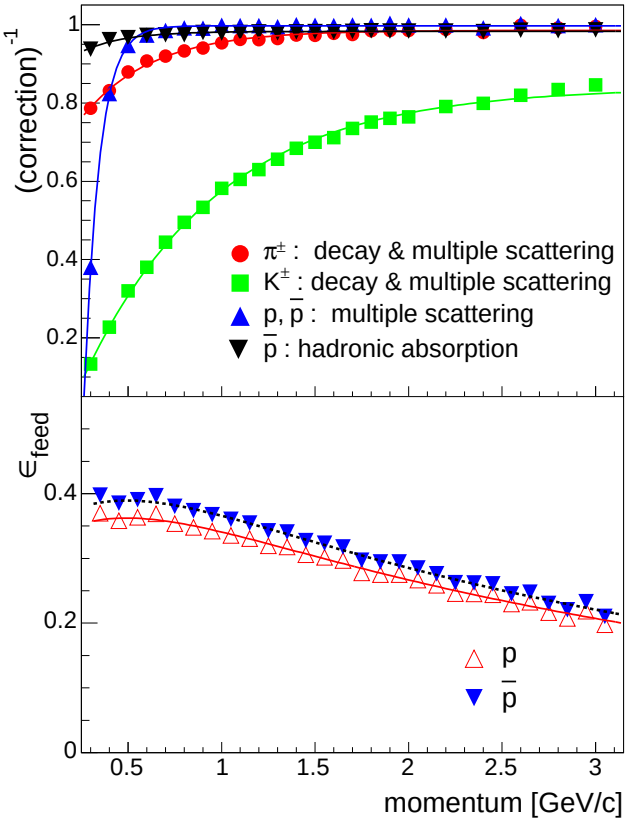

FIG. 4: Correction factors applied to the invariant yields, as discussed in the text. The top panel shows the momentum dependence of the multiple scattering, decay in flight and hadronic absorption effects. The bottom panel shows the fractional factors of p and $\overline{p}$ from Λ and $\bar{\Lambda}$ in all measured p and $\overline{p}$, ϵ_{feed}, as a function of momentum. The solid line displays $\frac{\Lambda \to p}{(\Lambda \to p)+p}$ and the dotted one shows $\frac{\bar{\Lambda} \to \overline{p}}{(\bar{\Lambda} \to \overline{p})+\overline{p}}$.

The multiplicity dependent track reconstruction efficiency has been studied by embedding simulated tracks into real tracks at the raw data level [22]. The combined events are reanalyzed to determine if the embedded tracks are still reconstructed by the tracking program.

Each track is associated with a number of pads in TPM1 and TPM2. The resulting tracking efficiency is parameterized as a function of the number of track-related pads found in the two TPCs with signals above threshold for pions, kaons, and protons in various spectrometer angle settings. The mean number of track-related pad hits in the data sample varies from ∼60−350 as the centrality varies from 0−60%. For the most central events, track reconstruction efficiency is ∼85−95% depending on spectrometer angle setting.

The efficiency for individual TOFW slats is investigated by projecting TPC tracks to the slat and comparing this to the distribution of TOFW hits. The possibility of having multiple hits on a single slat is also corrected for. No slat dependence is observed and the overall TOFW efficiency is ∼90%.

The single track efficiency as a function of momentum in the spectrometer is determined by a Monte Carlo simulation. Events with one particle are first processed through BRAG with multiple scattering, decays, and hadronic interactions processes included. In order to evaluate these effects, the simulated events are processed through the same digitization, reconstruction and particle selection algorithm that is applied to the real data. The upper panel of Fig. 4 shows correction factors applied to the pion, kaon and proton spectra at y=0 to account for multiple scattering and (π and K) decay in flight. The low momentum $\overline{p}$ spectra are also corrected for hadronic absorption in the beam pipe and detector materials. This effect amounts to $\sim 2-3\%$ of the total yield. The difference of correction factors at different spectrometer settings is below 1%.

Protons and antiprotons from weak decays lead to a contamination of the primary hadron spectra. The proton and antiproton spectra are corrected to remove the feed down contributions from Λ and $\bar{\Lambda}$ weak decays. At midrapidity the ratio $N(\Lambda) = 0.89N(p)$, $N(\bar{\Lambda}) = 0.95N(\bar{p})$ has been reported [23]. We take these ratios and measured spectra shapes as input to the BRAG for feed down correction from Λ decays. The simulated tracks are generated for the full phase space, digitized, and go through the real data analysis algorithm, as is done to determine the other correction factors. The lower panel of Fig. 4 shows the ratio (ϵ_{feed}) of secondary p and $\overline{p}$ to all measured p and $\overline{p}$ as a function of momentum. The fractional factors range from 10−35%, and the largest value is ∼35% around a momentum $p \sim 1$ GeV/c. We multiply the proton and antiproton spectra by $1-\epsilon_{feed}$ for all centrality windows and rapidities as a function of momentum. The data are corrected on a track-by-track basis for efficiency and feed down contributions.

III. EXPERIMENTAL RESULTS

Figure 5 shows the invariant spectra for charged hadrons, $\pi^{\pm}$, $K^{\pm}$, p, and $\bar{p}$ at different collision centralities. The overlaid lines indicate fits to the data from $y = 0$ in the range shown. The pion spectra are fitted with a power-law function, $A(1 + p_T/p_0)^{-n}$. For kaons the spectra are best fit by an an exponential in m_T , A$[e^{-m_T/T}]$, where $m_T = \sqrt{p_T^2 + m_0^2}$ where m_0 is the mass of the particle. The proton and antiproton m_T-spectra tend to deviate from a single exponential shape, so a sum of two exponential functions is used to in the fit. The point-to-point systematic uncertainties on the spectra and quality of fit are estimated by using other fit functions and varying the fit ranges. The errors shown on the data points are statistical only. The overall systematic errors are estimated to be 10−15%. The main sources for the overall systematic errors are from the uncertainties in the normalizations used to calculate the invariant yields. Others are from uncertainties in estimating background contribution, track reconstruction efficiencies, acceptance of spectrometer and particle identification losses. The yields and mean transverse momentum values are extracted from the fit functions. Tables II gives the fit ranges and the estimated percentage of the total yield included in the fit ranges.

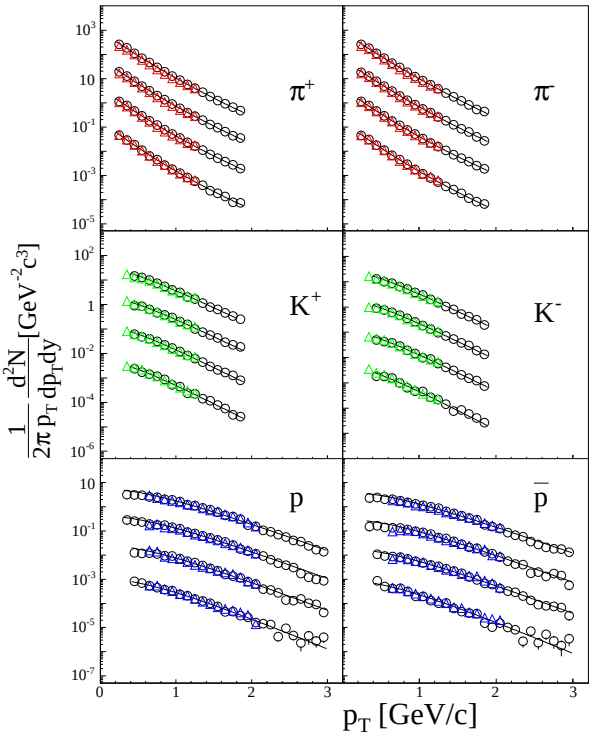

FIG. 5: The invariant yield spectra for the identified particles for the 0−10%, 10−20%, 20−40%, and 40−60% central collisions in Au+Au collisions at $\sqrt{s_{NN}}$=200 GeV. Circle(triangle) symbols are the results at $y = 0$ ($y \sim 1$). Curves overlaid to the data points are fits to the $y = 0$ data, as discussed in the text. For clarity, the data points are scaled down by a factor of 10 successively from the top (0−10%) to bottom(40−60%) in decreasing order of centrality. The error bars are statistical only.

	$y = 0$	$y \sim 1$
$\pi^{\pm}$	$0.2 < p_T < 1.9$ (76.5%)	$0.3 < p_T < 1.3$ (72.1%)
$K^{\pm}$	$0.4 < p_T < 1.9$ (48.0%)	$0.3 < p_T < 1.3$ (40.9%)
$p, \bar{p}$	$0.3 < p_T < 3.0$ (72.1%)	$0.6 < p_T < 2.1$ (64.9%)

TABLE II: Fit ranges for curves shown in Fig. 5. The yields were calculated from the data within the fit ranges, and the estimated percentage is the ratio of measured yields within the fit ranges to extrapolated yields for the full momentum range.

Figure 6 shows the mean transverse momenta, $\langle p_T \rangle$, as a function of N_{part}. We find that $\langle p_T \rangle$ increases with particle mass and centrality. This is suggestive of a hydrodynamic system where the initial pressure increases with the number of participants.

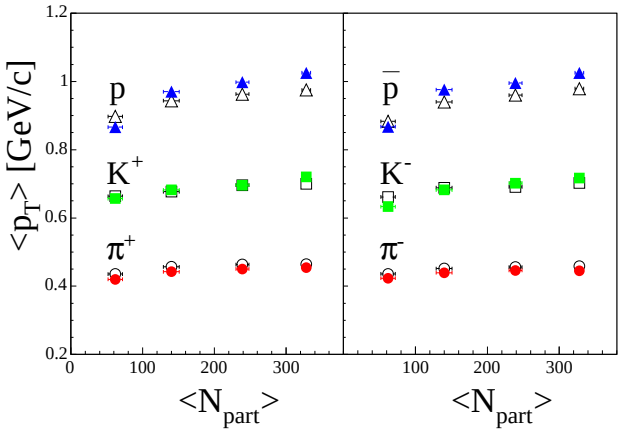

FIG. 6: Mean p_T extracted from the fit functions to the spectra as a function of centrality (N_{part}) for π^+, K^+, p (left) and π^-, K^-, $\bar{p}$ (right). Open symbols represent at $y = 0$, and closed symbols are for $y \sim 1$. The error bars are statistical only.

We also tried a hydrodynamic model fit to the experimental data with two free parameters: collective transverse flow velocity β and the global thermal freeze-out temperature T_f. We have utilized a version of a hydrodynamically inspired "blast-wave" model initially developed to describe lower energy data [11]. Assuming kinetic freeze-out of matter at constant T_f with a collective transverse flow characterized by a velocity β_s, the invariant m_T distribution can be described as follows:

$$\frac{dN}{m_T\, dm_T} \propto \int_0^{R_{max}} r\, dr\, m_T I_0\left(\frac{p_T \sinh\rho}{T_f}\right) K_1\left(\frac{m_T \cosh\rho}{T_f}\right), \quad (1)$$

where T_f is the freeze-out temperature, I_0, K_1 are modified Bessel functions and $\rho = \tanh^{-1}\beta_T$ is the transverse rapidity. The transverse velocity profile β_T is parameterized by the surface velocity β_S : $\beta_T(r) = \beta_S(r/R_{max})^{\alpha}$. Results of a simultaneous fit for 0−10% centrality of Eq. 1 to the spectra for $y = 0$ is shown in Fig. 7. The parameters α, T_f, and β_S were allowed to vary, as well as the normalization constants for each particle type and adjusted. The p_T coverage of spectra at $y \sim 1$ is not sufficient for a reliable hydrodynamic model fit. The source parameter used was $R_{max} = 13$ fm [24]. The integral in Eq. 1 is relatively insensitive to changes in R_{max}, changing by less than 5% when R_{max} is changed from 5 to 20 fm.

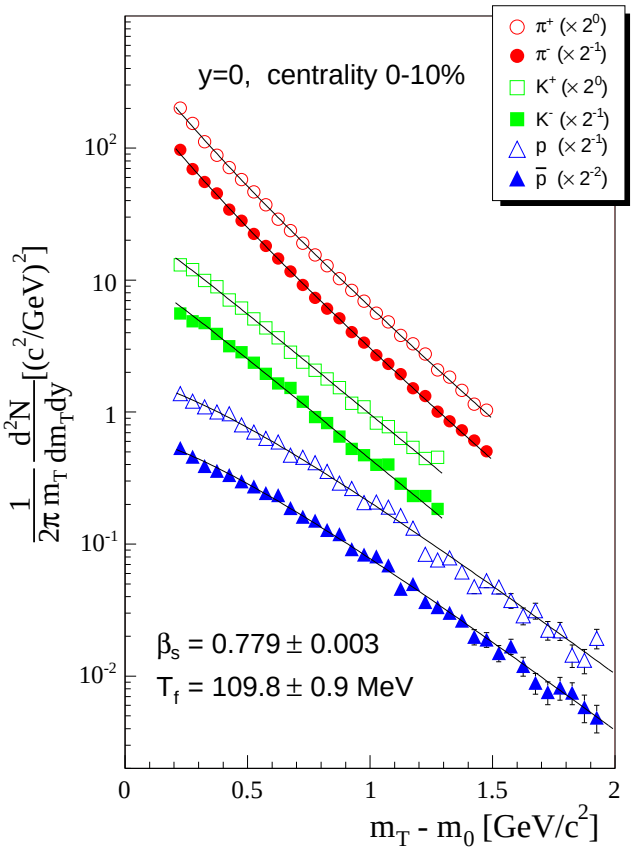

FIG. 7: The parametrization and the m_T spectra for 0-10% centrality The errors in the fit parameters are statistical only.

For the most central events (0−10%), the fit yields values of $T_f = 109.8 \pm 0.9$ MeV, $\beta_S = 0.779 \pm 0.003$, and $\alpha = 0.4 \pm 0.05$. The average flow velocity $\langle \beta_T \rangle$ is then estimated to be 0.65 by taking an average over the transverse geometry [25]. When fitting spectra from the other centrality windows we fixed the value of α to be 0.4. The fits in the four centrality bins give a χ^2/DOF between 1.3−1.45. The systematic uncertainties in the fit parameters are estimated to be less than 5%. Figure 8 shows the centrality dependence of the temperature and surface velocity. T_f decreases with centrality while increases β_s. Since the surface velocity keeps increasing until the system decouples these results suggest that central collisions decouple later. The increased energy associated with the surface velocity requires a lower final temperature by en-

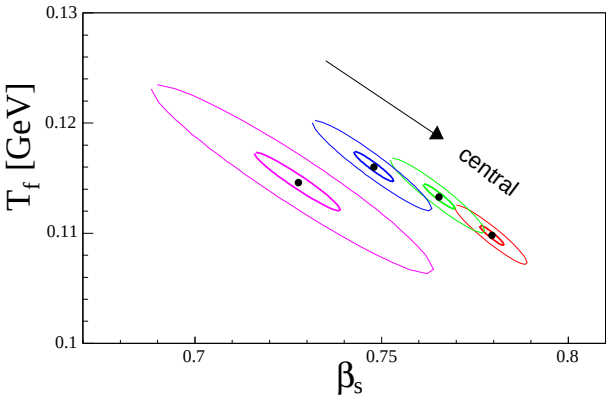

FIG. 8: Kinetic freeze-out temperatures T_f and transverse flow velocities β_s resulting from a simultaneous fit of to $\pi^{\pm}$, $K^{\pm}$, p and $\bar{p}$ spectra to Eq. 1 as a function of collision centrality. The points represent the best fit values of T_f and β_s while the contours indicate 1σ and 3σ levels. The systematic errors are $\leq 5\%$ and are not included in the figure.

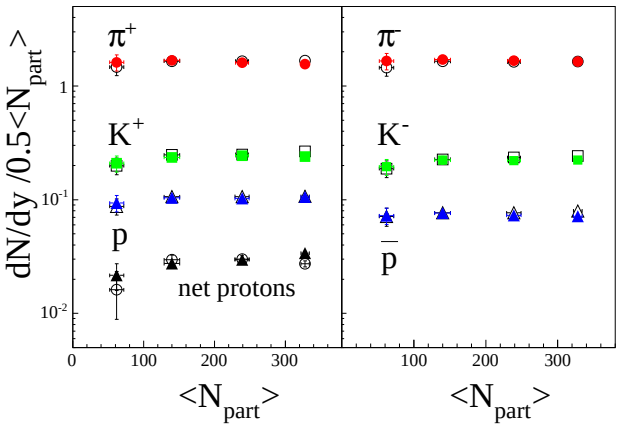

FIG. 9: Rapidity density (dN/dy) per participant pair ($N_{part}/2$) as a function of N_{part} for π^+, K^+, p, net proton (left) and π^-, K^-, $\bar{p}$ (right). Open symbols represent at $y = 0$, and closed symbols are for $y \sim 1$. The error bars represent the statistical errors only.

ergy conservation [26].

$y = 0$	$0-10\%$	$10-20\%$	$20-40\%$	$40-60\%$
π^+	274.6 ± 2.1	192. ± 1.7	115.6 ± 1.2	45.5 ± 0.84
π^-	268.5 ± 2.1	188.7 ± 1.7	115.1 ± 1.2	44.9 ± 0.81
K^+	43.8 ± 0.67	29.1 ± 0.54	17.4 ± 0.4	6.2 ± 0.26
K^-	39.6 ± 0.62	27.1 ± 0.52	15.8 ± 0.35	5.8 ± 0.25
p	17.5 ± 0.20	12.7 ± 0.16	7.4 ± 0.11	2.7 ± 0.08
$\bar{p}$	13.0 ± 0.17	9.2 ± 0.13	5.4 ± 0.09	2.2 ± 0.19
$y \sim 1$	$0-10\%$	$10-20\%$	$20-40\%$	$40-60\%$
π^+	255.4 ± 1.82	185.8 ± 1.60	117.4 ± 1.18	50.1 ± 0.89
π^-	269.4 ± 2.25	193.3 ± 1.91	119.4 ± 1.29	51.4 ± 0.10
K^+	39.1 ± 0.28	28.3 ± 0.25	16.5 ± 0.16	6.5 ± 0.11
K^-	36.7 ± 0.29	25.7 ± 0.25	15.5 ± 0.17	6.0 ± 0.12
p	17.3 ± 0.16	12.3 ± 0.14	7.3 ± 0.01	2.9 ± 0.11
$\bar{p}$	11.8 ± 0.15	8.7 ± 0.14	5.3 ± 0.08	2.2 ± 0.08

TABLE III: The yield dN/dy from integration of extrapolated function in each centrality bin at y=0 and $y \sim 1$. The fit range was shown in Tables II. The errors are statistical only.

The rapidity densities dN/dy are determined for each particle by integrating the measured p_T spectrum over p_T using the previously discussed functional form to extrapolate outside of the region of the measurement. Table III shows the results at $y = 0$ and $y \sim 1$, respectively. The dN/dy values per participant pair are shown as a function of N_{part} in Fig. 9. The systematic errors on the yields and $\langle p_T \rangle$ values are from the extrapolation to the low momentum region and are estimated as 5−10%. The only centrality dependence evident is a small increase in the rapidity densities for the K and p channels in going to more central collisions. The net proton rapidity densities show a increase from 40−60% to 20−40% and saturate after that. The fractions of protons produced by stopping, $(N_p - N_{\overline{p}})/((N_p + N_{\overline{p}})$, are 0.15±0.01 at $y = 0$ and 0.19±0.01−0.13±0.03 at $y \sim 1$ from peripheral to central collisions. Our $\overline{p}/p$ ratio from pp collisions showed a proton excess of 12% at midrapidity [27]. This baryon asymmetry has been modeled at lower energy systems [28] where it has been found to be significant greater [29, 30].

Figure 10 compares the K/π ratios as a function of p_T for central and peripheral collisions. The ratios for both charges increase with p_T at both rapidities. There is no significant centrality dependence below 1 GeV/c, however, the increase is faster in central than peripheral collisions at higher momentum. The weak centrality dependence of the K/π production at RHIC [31] differs from the measurements at lower energy from AGS [32] and SPS experiments [33], where the K^-/π^- ratio is enhanced ($\sim 1.5-2$) from central collisions compared to peripheral collisions. This might be attributed to the energy dependent longitudinal geometry of the colliding nuclei [34, 35], but a further experimental and theoretical work is needed to understand the observed energy dependence.

Figure 11 shows the p/π^+ and $\overline{p}/\pi^-$ ratios as a function of p_T obtained at $y = 0$ and $y \sim 1$ for central and peripheral collisions. For both centralities the ratios rise fast at low p_T and then tend to saturate. Around $p_T \sim 2.0$ GeV/c the ratios increase from peripheral to central collisions by 30% for p/π^+ and by 50% for $\overline{p}/\pi^-$ ratios. Parton recombination and quark coalescence models describe qualitatively the observed baryon to meson ratios in the intermediate p_T region [36, 37].

To clarify the centrality dependence of particle ratios at higher p_T, and to see if the ratios of harder particles are sensitive to the size of the interaction volume, we present the K/π and p/π ratios versus N_{part}. Figure 12 shows the K/π and p/π ratios for $1.2 < p_T < 2.0$ GeV/c increase with N_{part}. This increase is stronger for protons than for kaons with little difference in slope between the

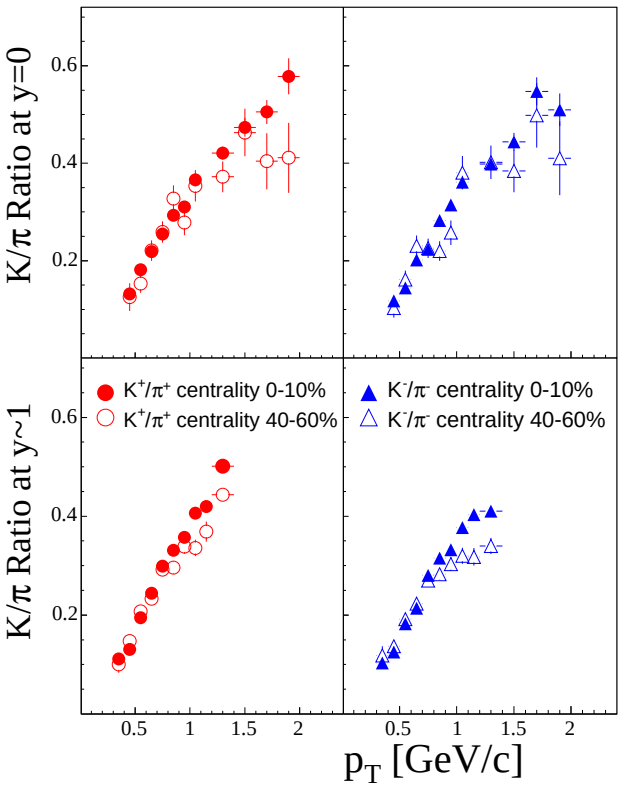

FIG. 10: K^+/π^+ (left) and K^-/π^- (right) ratios as a function of p_T at $y = 0$ (top) and $y \sim 1$ (bottom). Closed and open symbols represent central (0−10%) and peripheral (40−60%) collisions, respectively. Only statistical error bars are shown.

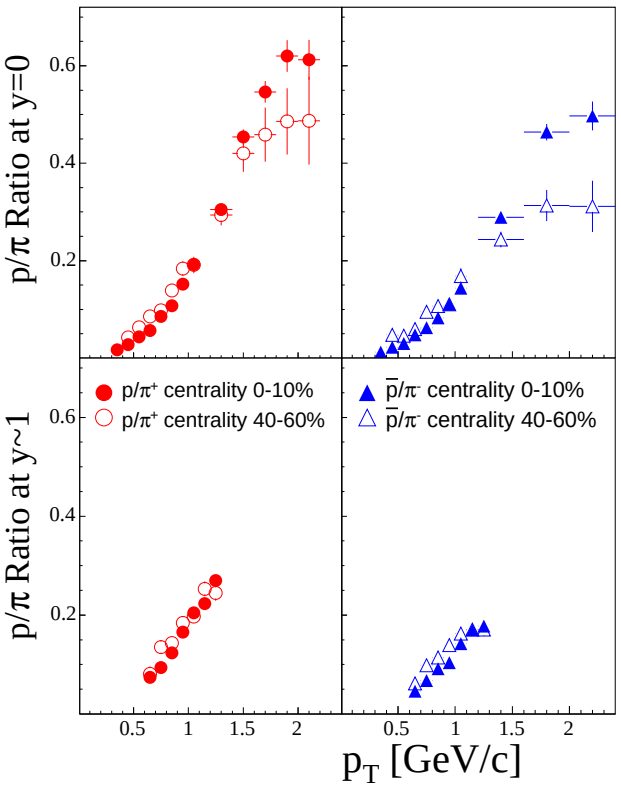

FIG. 11: p/π^+ (left) and $\bar{p}/\pi^-$ (right) ratios as a function of p_T at $y = 0$ (top) and $y \sim 1$ (bottom). Closed and open symbols represent central (0−10%) and peripheral (40−60%) collisions, respectively. Only statistical error bars are shown.

particle and antiparticle ratios. This hierarchy in mass may reflect transverse flow. A common velocity field will have a stronger effect on the p_T distribution of heavy particles than of light ones. We expect that the strength of the transverse velocity should increase with centrality and this is consistent with our data, as shown in Fig. 8. However, we would also expect the increase of particle ratios with N_{part} in this p_T region may also be consistent with coalescence approach.

IV. SUMMARY

Particle production of identified charged hadrons, $\pi^{\pm}$, $K^{\pm}$, p, and $\bar{p}$ in Au+Au collisions at $\sqrt{s_{NN}} = 200$ GeV has been studied as a function of transverse momentum and collision centrality at $y = 0$ and $y \sim 1$ by the BRAHMS collaboration at RHIC. Significant collective transverse flow at kinetic freeze-out is observed for both central and mid-central events. The magnitude of the radial expansion increases with the collision centrality indicating more hydro-like collectivity in the transverse direction for the central collisions. The p, $\overline{p}$ and $K^{\pm}$ yields relative to the pion production at RHIC show a strong transverse momentum dependence. Contrary to lower

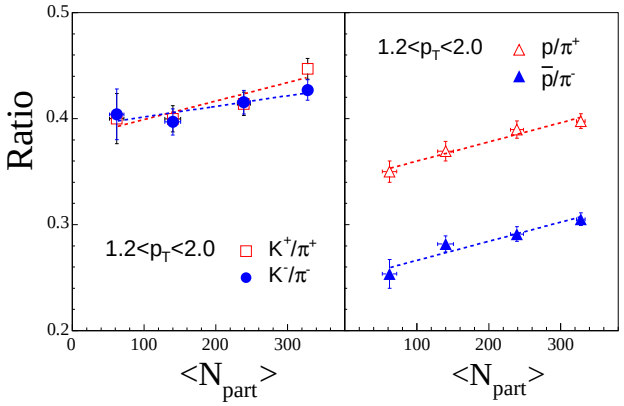

FIG. 12: The ratio of K/π (left) and p/π (right) as a function of N_{part} for $1.2 < p_T < 2.0$ GeV/c at mid-rapidity. Open and closed symbols represent the ratio of positive particles and negative ones, respectively.

energy results no significant centrality dependent K/π ratios below 1 GeV/c are observed at the RHIC energy. The p/π^+ and $\overline{p}/\pi^-$ ratios increase with p_T and centrality reaching a value of 0.6 at $p_T = 2$GeV/c. The particle yield scaled by N_{part} is nearly constant, and only weakly increasing with centrality for all particles. No significant

changes for the bulk properties in hadron production are observed within one unit around midrapidity in Au+Au collisions at $\sqrt{s_{NN}} = 200$ GeV.

Acknowledgments

This work was supported by the division of Nuclear Physics of the Office of Science of the U.S. DOE, the Danish Natural Science Research Council, the Research Council of Norway, the Polish State Committee for Scientific Research and the Romanian Ministry of Education and Research. We thank the staff of the Collider-Accelerator Division of BNL for their excellent and dedicated work to deploy RHIC and their support to the experiment.

[1] For a review see E.Shuryak, Phys. Rep. **61**, 71 (1980) and **115**, 151 (1984).
[2] H. Satz, Rep. Prog. Phys. **63**, 1551 (2000).
[3] P. Jacobs and X. N. Wang, hep-ph/0405125.
[4] I. Arsene *et al.*, BRAHMS Collaboration, submitted to Nucl. Phys. A arXiv.org/abs/nucl-ex/0410020
[5] B.B.Back *et al.*, PHOBOS Collaboration submitted to Nucl. Phys. A (2004). arXiv.org/abs/nucl-ex/0410022
[6] K. Adcox *et al.*, PHENIX Collaboration submitted to Nucl. Phys. A (2004). arXiv.org/abs/nucl-ex/0410003
[7] J. Adams *et al.*, STAR Collaboration submitted to Nucl. Phys. A (2004). arXiv.org/abs/nucl-ex/0501009
[8] R. Koch, B. Müller, and J. Rafelski, Phys. Rep. **142**, 167 (1986).
[9] I.G. Bearden *et al.*, BRAHMS Collaboration, Phys. Rev. Lett. **93**, 102301 (2004).
[10] S. A, Bass, B, Müller, and D. K. Srivastava, Phys. Rev. Lett. **91**, 052303 (2003).
[11] E. Schnedermann, J. Sollfrank, and U. Heinz, Phys. Rev. **C48**, 2462 (1992).
[12] BRAHMS Publication Figures and Data Archive, http://www4.rcf.bnl.gov/brahms/WWW/publication-data.
[13] ELECTRONIC PHYSICS AUXILIARY PUBLICATION SERVICE.
[14] I.G. Bearden *et al.*, BRAHMS Collaboration, Phys. Rev. Lett. **88**, 202301 (2002).
[15] Y.K Lee *et al.*, Nucl. Instr. and Meth. **A516**, 281 (2004).
[16] M. Adamczyk *et al.*, BRAHMS Collaboration, Nucl. Instr. and Meth. **A499**, 437 (2003).
[17] X.N. Wang and M. Gyulassy, Phys. Rev. **D44**, 3501 (1991), http://www-nsdth.lbl.gov/ xnwang/hijing/
[18] P. L. H. Christiansen, PhD thesis, Niels Bohr Institute, University of Copenhagen, 2003.
[19] B. H. Samset, Master's thesis, University of Oslo, 2001.
[20] J. I. Jørdre, Master's thesis, University of Bergen, 2000.
[21] *GEANT 3.21*, CERN program library.
[22] T. M. Larsen, Master's thesis, University of Oslo, 2002.
[23] K. Adcox *et al.*, PHENIX Collaboration, Phys. Rev. Lett. **89**, 092302 (2002).
[24] F. Retiere *et al.* nucl-ex/0111013 (2001).
[25] S. Esumi, S. Chapman, H. van Hecke, and Nu Xu, Phys. Rev. **C55**, R2263 (1997).
[26] P. Kolb and U. Heinz, nucl-th/0305084 (2003)
[27] I.G. Bearden *et al.*, BRAHMS Collaboration, Phys. Lett. **B607**, 42 (2005).
[28] D. Kharzeev, Phys. Lett. **B378**, 238 (1996).
[29] B. Alper *et al.*, Phys. Lett. **B47**, 275 (1973).
[30] A.M. Rossi *et al.*, Nucl. Phys. **B84**, 269 (1975).
[31] C. Adler *et al.*, STAR Collaboration, Phys. Lett. **B595**, 143 (2004).
[32] L. Ahle *et al.*, E802 Collaboration, Phys. Rev. **C60**, 044904 (1999).
[33] F. Sikler *et al.*, NA49 Collaboration, Nucl. Phys. **A661**, 45c (1999).
[34] F. Wang, J. Phys. **G28**, 2109 (2002).
[35] I.G. Bearden *et al.*, BRAHMS Collaboration, nucl-ex/0403050, submitted to Phy. Rev. Lett.
[36] R. C. Hwa and C. B. Yang, Phys. Rev. **C67**, 034902 (2003).
[37] V. Greco, C. M. Ko and P. Lévai Phys. Rev. Lett. **90**, 202302 (2003).